

https://dspace.org/

Internal fields in diamond and related materials

Connell, Simon Henry

2015-02-13
http://hdl.handle.net/10539/16997

Downloaded from a DSpace repository. https://dspace.org/

flashed onto it. This provided an earthing contact to prevent charge build-up steering instabilities and also served to increase the PMT light collection by reflection.

Fig. 4.4 shows a timing spectrum obtained by a singles measurement of the 110 keV γ - rays from ^{19}F in a thick CaF_2 target with respect to the signal from the "halo" detector. The decay constant of the 110 keV state is 0.85 ns. The spectrum should reflect the structure of the beam pulsing. Computer analysis of the spectrum shows the nett time resolution to be 4 ns and ratio of the background integrated between pulses to the pulse area to be 5%. The decay component observable in Fig. 4.4 is due to Compton events originating from the longer living 197 keV state slipping through the energy windows.

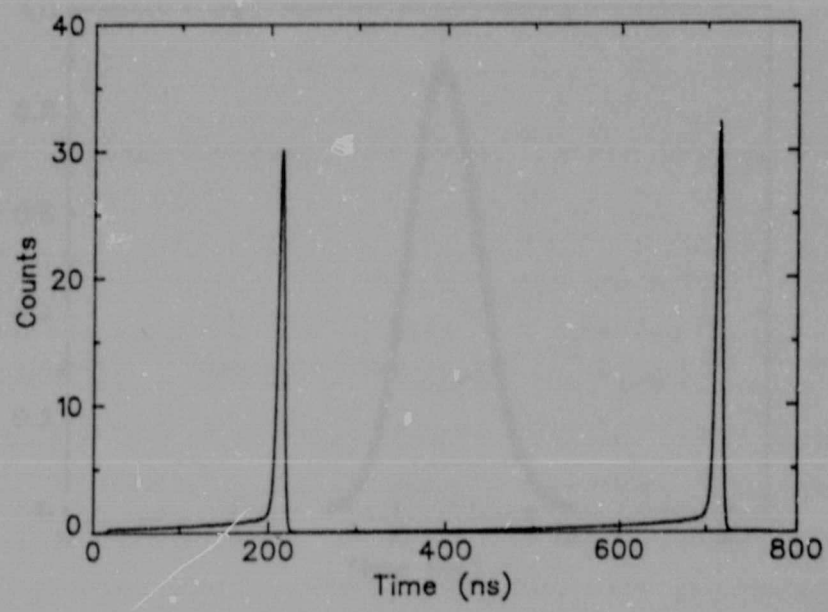


Fig. 4.4 Beam pulsing profile.

Data capture

Detectors

At least two detectors, one at 0°, the other at 90°, are necessary for a TDPAD

experiment. The detectors used in this experiment were NaI(Tl) crystals, 50 mm × 44 mm ⌀, coupled to Phillips photo-multiplier tubes, XP2020, with a modified base to improve the timing signals (at the expense of some energy resolution). Fig. 4.5 shows an off-line timing spectrum using 511 keV annihilation radiation from a ^{22}Na source. At this energy the timing resolution is (FWHM) 2.55 ns. Fig. 4.6 shows a typical energy spectrum of the ^{19}F as it appears during a TDPAD measurement. In this case it is from recoil implanted ^{19}F in diamond IIa. The energy resolution at the 197 keV level is 10%. This represents an impressive performance from NaI crystals of this size. The timing output was taken direct from the anode pulse, which had a rise time of 2.3 ns and its magnitude for 197 keV γ - rays was about 150 mV.

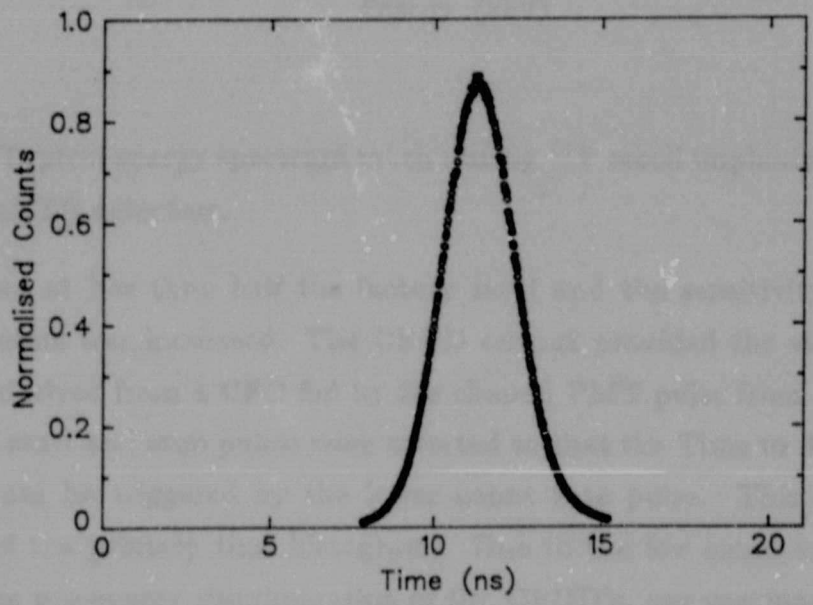


Fig. 4.5 Timing spectrum from the two NaI(Tl) detectors using a ^{22}Na source.

Electronics

The electronic signal processing circuitry is shown in Fig. 4.7. The Constant Fraction Differential Discriminators (CFDD) trigger directly off the anode pulse. In order to enable the triggering from weak signals while still having the fast discriminator energy windows near the middle of their range, the module was modified to trigger on

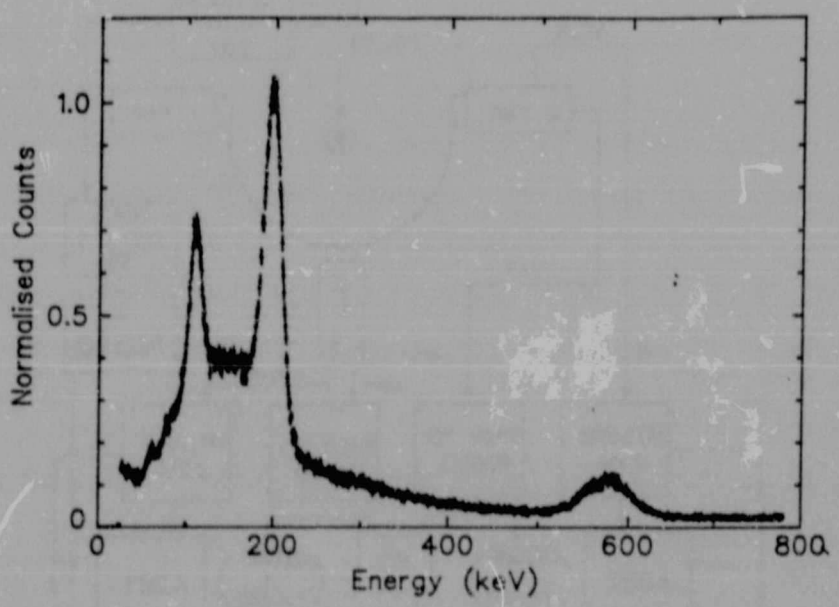


Fig. 4.6 Typical energy spectrum taken during ^{19}F recoil implantation into diamond using NaI(Tl) detectors.

input pulses at less than half the factory level and the sensitivity of the front panel potentiometers was increased. The CFDD output provided the stop pulse. The start pulse was derived from a CFD fed by the shaped PMT pulse from the "halo" detector. In fact the start and stop pulses were inverted so that the Time to Amplitude Converter (TAC) would be triggered by the lower count rate pulse. This explains the lateral inversion of the primary time histograms. Due to the low count rate presented to the TAC by the pre-energy discrimination of the CFDD's, use was made of only one TAC. This ensured the same baseline for both 0° and 90° spectra. The spectra were separated afterwards at the Analogue to Digital Converter (ADC) by routing based on the analysis of the slow energy signal. The TAC was operated in the external strobe mode, with the external strobe logic pulse provided by the TSCA on the slow energy signal. If the two γ detectors fired in coincidence, then the TAC would recieve a reset pulse. For the rest conventional slow-fast circuitry was used [Ar 80]. The energy spectra of each NaI detector as gated by either the CFDD's on the fast windows or the Timing Single Channel Analysers (TSCA) on the slow windows were displayed continuously for test and monitoring purposes. The Data Acquisition System was a software driven Multi-

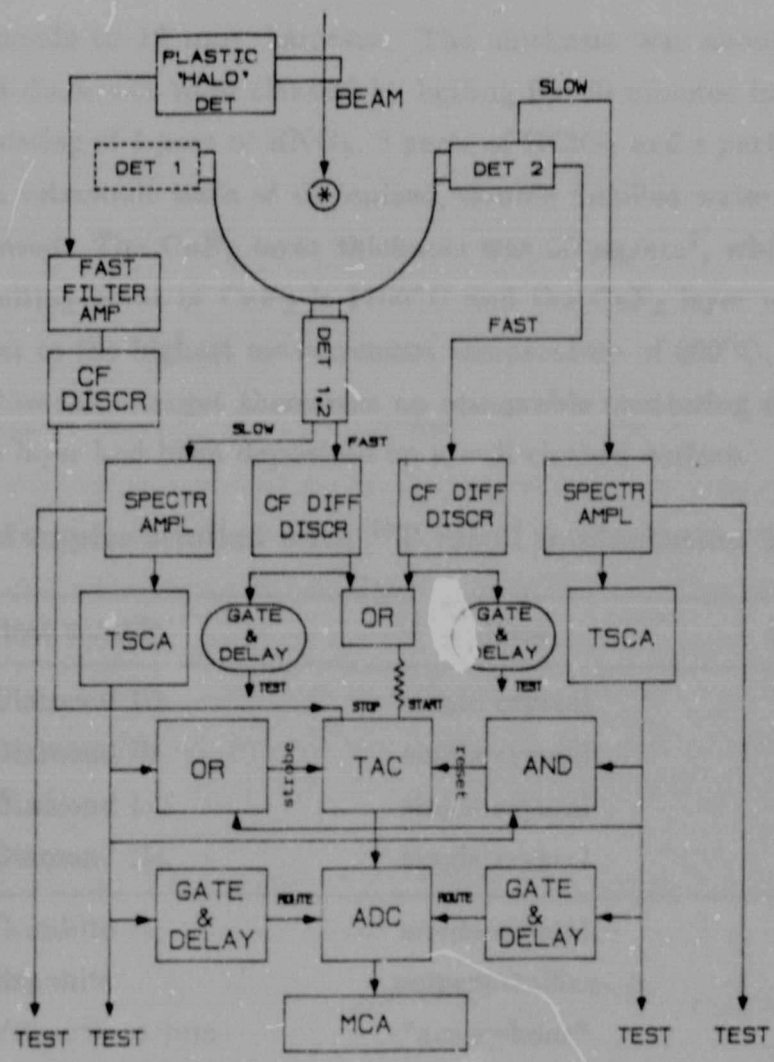


Fig. 4.7 Circuit diagram for the TDPAD signal processing.

Channel Analyser (Nuclear Data's μMCA) which was controlled via an Olivetti M24 personal computer equipped with a 16-colour enhanced graphics display.

Targets

Preparation

The list of TDPAD targets studied, their crystalline state and the cleavage plane of the mainface is presented in Table 4.1 below. All of the targets were discs, constructed by cleaving or machining and polishing. The sizes ranged from 6 mm diameter for the

smaller diamonds to 12 mm diameter. The thickness was about 2 mm in all cases. The polished diamonds were cleaned by boiling for 30 minutes in a concentrated acid mixture consisting of 1 part of HNO_3, 3 parts of $HClO_3$ and 4 parts of H_2SO_4 and then rinsing in an ultrasonic bath of de-ionized, double distiiled water. The other samples were only rinsed. The CaF_2 layer thickness was 30 $\mu g/cm^2$, which corresponds to .1 μm. The melting point of CaF_2 is 1700°C and the CaF_2 layer was found to be very stable at least to the highest measurement temperature of 600°C. Even after 3 days of running on the same target there was no observable sputtering effect. This was true provided the layer had been deposited on a well cleaned surface.

Table 4.1 Samples studied with ^{19}F recoil implantation TDPAD.

Host sample	Lattice	Main face
Diamond IIb	single crystal	(111)
Diamond Ib	single crystal	(111)
Diamond Ia	single crystal	(111)
Diamond IIa	single crystal	(111)
Graphite	single crystal	-
Graphite	polycrystalline	-
Vitreous carbon	"amorphous"	-
Colloidal carbon	"amorphous"	-

The crystalline state was as determined by a mono-chromatic X-ray Laue pattern. Note that the X-ray technique is macroscopic and averages over the dimensions of the interrogating beam spot size of 4 mm. In contrast the TDPAD technique is microscopic and averages over at most the next nearest neighbour dimensions of a few Angstroms. This explains why samples labelled above as amorphous appeared polycrystalline to the TDPAD technique, and illustrates the controversy of the definition of amorphous.

There were three different target mounts.

1. A (θ, ϕ) articulating goniometer mount was used for room temperature and orientation dependent measurements.

2. A cold finger mount cooled by a liquid nitrogen reservoir was used for the low temperature measurements.

3. The heated sample holder was an extremely sophisticated device. It satisfied the requirements of electrical insulation for accurate measurement of beam current in the picoamp range, of thermal insulation from the delicate γ - ray exit windows, of extremely low power consumption and of no obstruction to the line of sight to the beam and detector. The electrical insulation requirement necessitated a floating power supply for which motor car batteries were used. The long running time of the measurement restricted the heating power to a maximum of 35 W. It was used to access temperatures up to 550° C. The sample was mounted against milled washers of molybdenum so that the correct orientation was achieved. The washer and target were strapped against a molybdenum spindle wound with thermocoax electrically insulated heater wire which was capable of temperatures up to 1200°C. Molybdenum heat shields protected the glue on the delicate γ windows from melting.

The targets were strapped into the mounts with aluminium or molybdenum strips, providing good thermal contact while not obstructing the line of sight to the beam or detector positions. The choice of materials was based on the requirement that no lines in the (p,p′) excitation spectrum should contaminate the region of the $^{19}F^*$ 197 keV peak. The molybdenum mount was chosen for the higher temperatures as the aluminium began to evaporate, destroying the electrical insulation. The goniometer and high temperature target mounts are shown in Fig. 4.8. The electrical leads shown are the thermocouple, heater leads and beam current lead.

Characterization

The diamond type was determined from infra-red absorption spectra. The crystallographic orientation of the diamond was determined from its X-ray Laue pattern. A protractor produced from a computer generated projection of the three dimensional geometry onto a plane was used to measure (from the Laue pattern) the polar and azimuthal angles of the low indice directions, $<100>$, $<110>$ and $<111>$, with respect to the main face of the diamond and the markings on it. The orientation of the diamond lattice with respect to the beam-detector geometry could then be set within

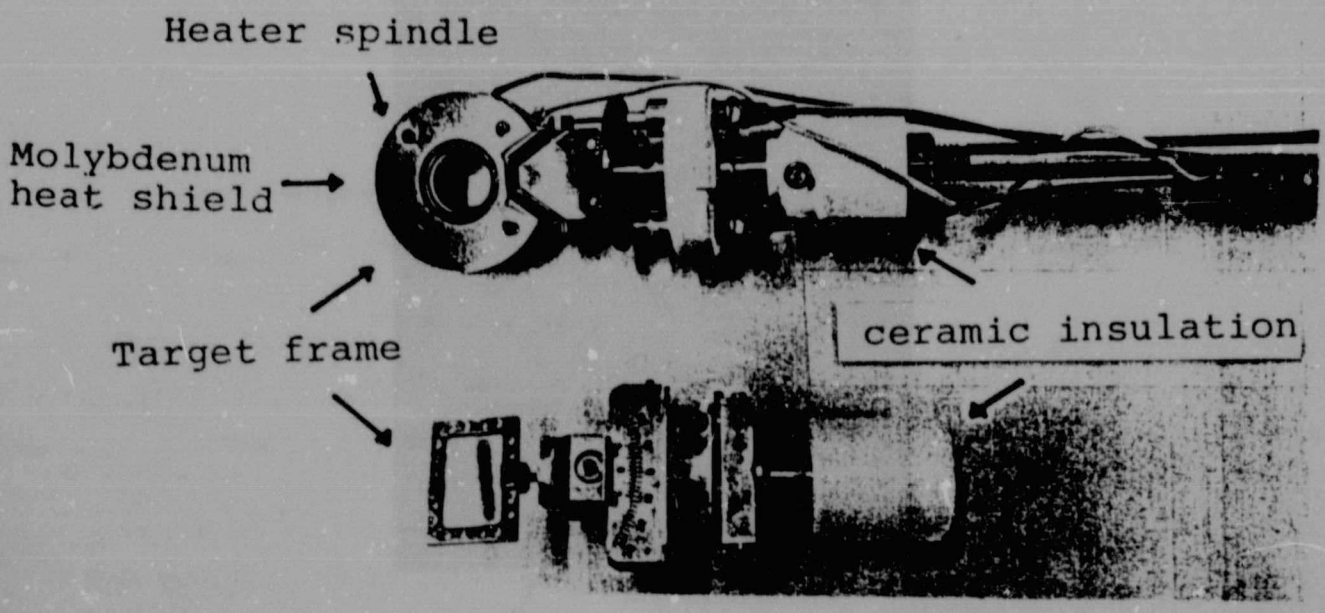


Fig. 4.8 The goniometer and high temperature target mounts.

3°. A model of the unit cell of the diamond lattice helped to decide which rotations would best achieve the desired orientation needed for the experiment. The sample was then mounted in the goniometer and the rotations carried out. A sample Laue pattern for a type IIa diamond is shown in Fig. 4.9. This 3-fold symmetry is consistent with the (111) plane. The directions of the $<100>$ and $<110>$ axis projected onto this plane have been labelled in the figure. A polar and azimuthal rotation of 8° and 14° respectively will bring the $<111>$ axis perpendicular to the cleavage plane.

Control

Fig. 4.10 and Fig. 4.11 represent tests of the TDPAD system using a thick CaF_2 target. Fig. 4.10 is the raw time histogram collected as described above. Fig. 4.11 is the analysis of this data as described in the previous chapter and the following sections. No electric field gradient is expected for ^{19}F at CaF_2 lattice sites. A TDPAD spectrum

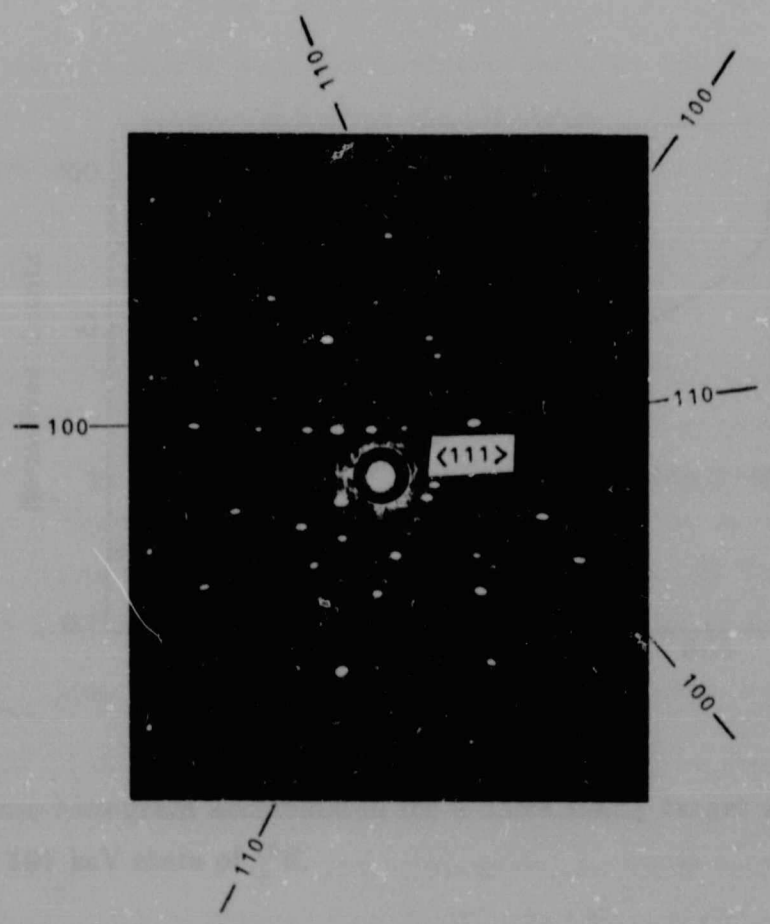


Fig. 4.9 Sample Laue pattern for single crystal diamond IIa.

of this substance should display no perturbation. It is clear that this is indeed the case. The TDPAD signals obtained when applying the method to other systems are thus properties only of the systems themselves. Note that CaF_2 is also a good choice for use as a probe containing evaporated layer as it will not interfere with signals from within the diamond lattice.

Data Reduction and Analysis

Primary data reduction

A typical run time for a TDPAD experiment was 50 hours. During this time the detector carriage was rotated clockwise or counter-clockwise every 4 hours by 90°, effectively interchanging the detector positions (see Fig. 4.7). Thus typically 4 classes of spectra, $N_i(1,0°,t)$, $N_i(1,90°,t)$ and $N_i(2,0°,t)$ and $N_i(2,90°,t)$ were generated in

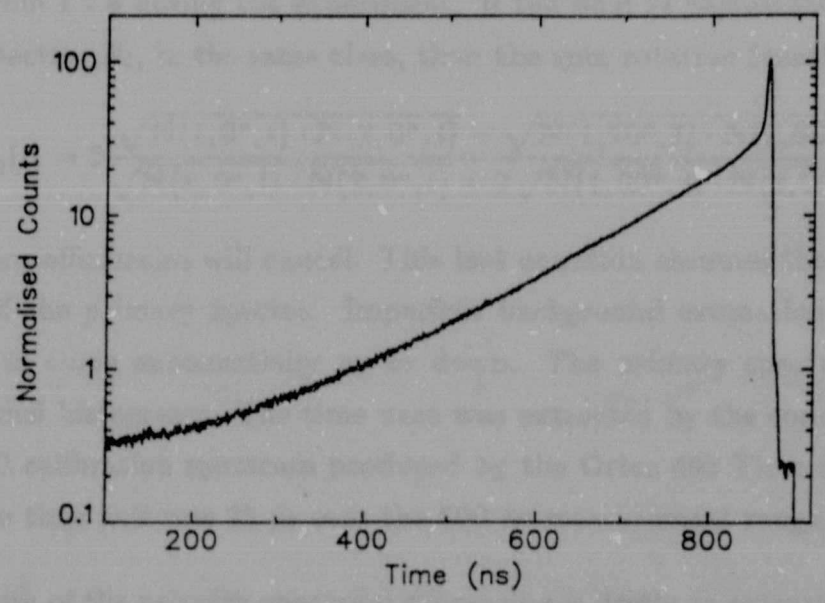


Fig. 4.10 Time histogram accumulated for a thick CaF_2 target showing only the decay of the 197 keV state of ^{19}F.

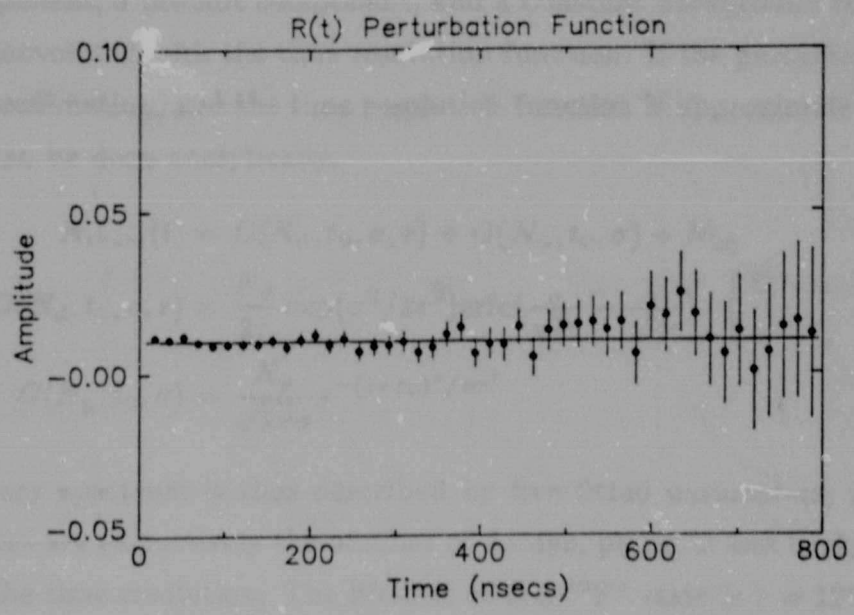


Fig. 4.11 Spin rotation spectrum for $^{19}F^*$ in a thick CaF_2 crystal showing no perturbation as expected.

pairs. The normal and interchanged positions are labelled 1 and 2 respectively, and the index i runs from 1 - 4 during the experiment. If the bold N represents the sum of all the primary spectra, N_i, in the same class, then the spin rotation function is

$$R_{\rm exp}(t) = 2\frac{\sqrt{\mathbf{N}(1,0°,t)\cdot\mathbf{N}(2,0°,t)} - \sqrt{\mathbf{N}(1,90°,t)\cdot\mathbf{N}(2,90°,t)}}{\sqrt{\mathbf{N}(1,0°,t)\cdot\mathbf{N}(2,0°,t)} + 2\sqrt{\mathbf{N}(1,90°,t)\cdot\mathbf{N}(2,90°,t)}}$$

and the detector efficiencies will cancel. This last equation assumes the background is stripped out of the primary spectra. Imperfect background estimation can cause the $R(t)$ function to slope exponentially up or down. The primary spectra were binned into 1024 channel histograms. The time base was extracted by the computer from the TAC and ADC calibration spectrum produced by the Ortec 462 Time calibrator. The accuracy of the time axis was 25 ps over the 500 ns measurement range.

The purpose of the primary spectrum processing is firstly to extract the time zeros t_0 of the $N_i(i,0°,t)$ so that spectra from the same class may be summed together, and secondly, once the $\mathbf{N}(i,0°,t)$ have been obtained, the background $N_{\rm bg}$ is fitted so that it can be stripped from the spectrum in preparation for construction of the $R(t)$ ratio. This is accomplished by modeling the spectrum as the sum of three contributions, a perturbed decay component, a prompt component, and a constant background component. All of these are convoluted with the time resolution function. If the perturbation is neglected in this approximation, and the time resolution function is approximated by a Gaussian, then this can be done analytically.

$$N_{\rm theor}(t) = D(N_{\rm d},t_0,\sigma,\tau) + G(N_{\rm p},t_0,\sigma) + N_{\rm bg}$$

$$D(N_{\rm d},t_0,\sigma,\tau) = \frac{N_{\rm d}}{2\tau}\exp(\sigma^2/2\tau^2)\mathrm{erfc}\left(\frac{\sigma}{\sqrt{2}\tau} - \frac{t}{\sqrt{2}\sigma}\right)\cdot\begin{cases}0, & t<t_0\\ e^{-t/\tau}, & t\geq t_0\end{cases}$$

$$G(N_{\rm p},t_0,\sigma) = \frac{N_{\rm p}}{\sqrt{2\pi}\sigma}e^{-(t-t_0)^2/2\sigma^2}$$

Each primary spectrum is thus described by five fitted parameters, $N_{\rm d}$, $N_{\rm p}$, $N_{\rm bg}$, t_0 and σ. These are respectively the number of decays, prompts and background, the time zero, and the time resolution. The lifetime of the $^{19}F^*$ state is $\tau = 128$ ns. This model is displayed schematically in Fig. 4.12 and a sample fit of the four classes of spectra is shown in Fig. 4.13.

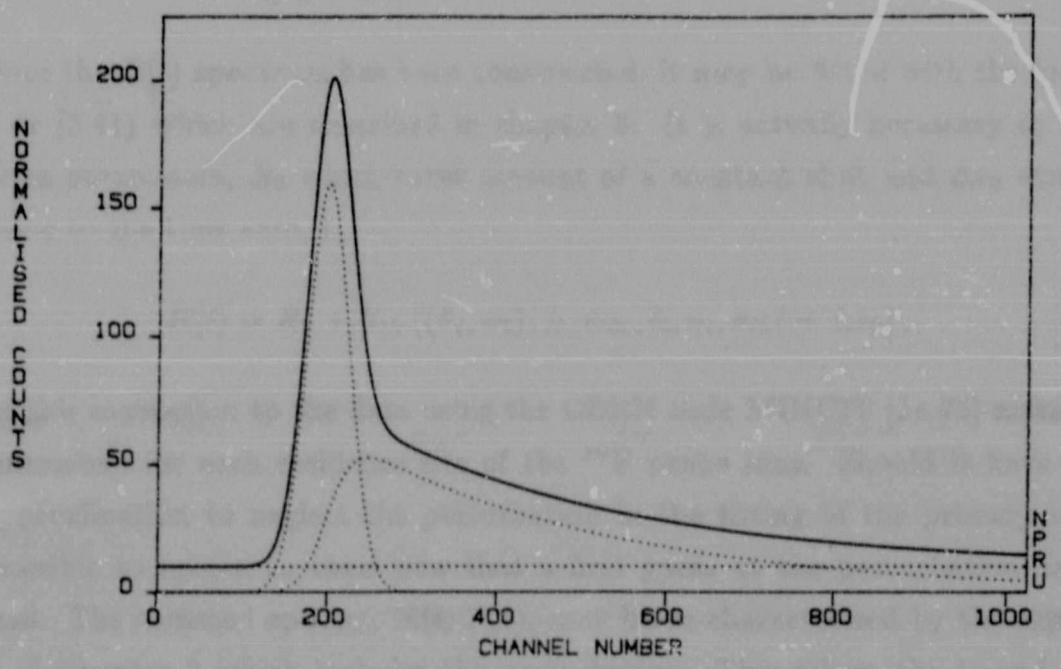


Fig. 4.12 Model function used to reduce the primary TDPAD spectra.

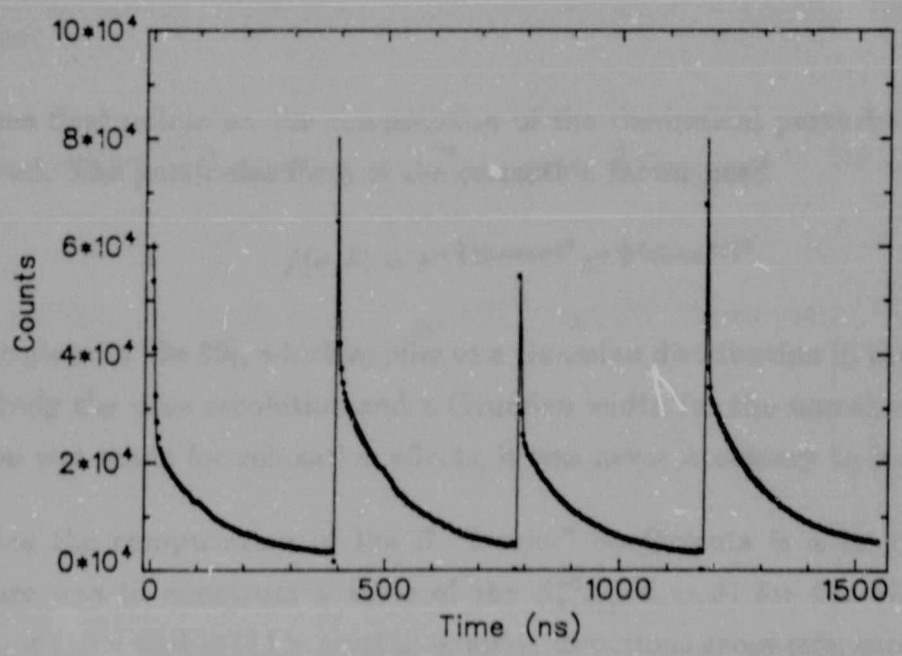


Fig. 4.13 The four classes of primary TDPAD spectra. The spectra showing the stronger perturbation are 0°spectra.

Extraction of the efg parameters

Once the $R(t)$ spectrum has been constructed, it may be fitted with the functions (3.39) or (3.41) which are described in chapter 3. It is actually necessary to include two extra parameters, R_0 which takes account of a constant shift and Δt_0 which is a correction to the time zero, t_0.

$$R(t) = R_0 + R_{\rm th}\left((\vartheta_i, \varphi_i), f_i, w_{0i}, \delta_i, \eta_i, \sigma_i; t + \Delta t_0\right).$$

Fitting this expression to the data using the CERN code MINUIT [Ja 75] extracts the efg parameters for each residence site of the ^{19}F probe ions. Should it have been a bad approximation to neglect the perturbation in the fitting of the primary spectra, it is possible to return to them now that a first guess at the perturbation has been obtained. The summed spectra, $\mathrm{N}(i, 0°, t)$, may be re-characterized by the expression (3.38) of Chapter 3 which includes the perturbation. This allows the t_0 and $N_{\rm bg}$ to be more accurately determined, and the analysis process can continue with a better reduction to $R_{\rm exp}(t)$. This iterative procedure is especially successful for cases where the perturbation is large and it results very quickly in a clean and accurate $R_{\rm exp}(t)$ reduction.

Some final points on the computation of the theoretical perturbation function are mentioned. The particular form of the correction factor used

$$f(\sigma, \delta) = e^{-\frac{1}{2}(\varrho_p \omega_0 \sigma)^2} e^{-\frac{1}{2}(\varrho_p \omega_0 \delta t)^2}$$

was that given in [Be 69], which applies to a Gaussian distribution in the efg. σ and δ are respectively the time resolution and a Gaussian width for the non-sharp efg. Although provision was made for relaxation effects, it was never necessary to include them.

Since the computation of the S "fourier" coefficients is a lengthy process, our procedure was to construct a table of the $S^{\rm eff}_{k_1 k_2 p}(\vartheta, \varphi, \theta)$ for the efg parallel to the <100>, <110> and <111> crystallographic directions cross-referenced with a variety of detector directions. Lagrangian fixed point interpolation on this table provided a fast computational method for construction of the $S^{\rm eff}_{k_1 k_2 p}(\vartheta, \varphi, \theta)$. The first Appendix provides more details on the construction of the $S^{\rm eff}_{k_1 k_2 p}(\vartheta, \varphi, \theta)$ coefficients.

CHAPTER 5.
RESULTS AND CONCLUSIONS (TDPAD)

Contents

Introduction 66

Residence Sites 68

Symmetry Property of Perturbation 86

Diamond Type Dependence 94

Cluster Calculations 109

Temperature Dependence 118

Other Carbon Allotropes 134

Introduction

This chapter represents a selection of the papers that resulted from the ^{19}F TDPAD investigations of diamond. What follows is a short description of each paper, depicting the progression the understanding and the development of the TDPAD technique using ^{19}F as probe, through to the interesting results that were extracted for the ^{19}F impurity in diamond.

The first paper, *Residence Sites for ^{19}F Ions Implanted into Diamond*, describes an orientation dependence study of ^{19}F recoil implantation into single crystal diamond. This was chosen as the first experiment in order to pin down the orientation of the efg principal axis. A type IIb diamond was used as this rare diamond has the purest lattice most free of defects. Two residence sites for the ^{19}F probe ions in diamond were found. The first has a quadrupole coupling frequency of $\approx$ 60 MHz, is well defined and has near axial symmetry for the efg. The second residence site has a lower quadrupole coupling frequency, but still near axial symmetry and is characterized by large spread in the efg. The efg was found to be along the <111> crystallographic direction for both sites.

Also described in the first paper is the theoretical fit function and the description of the generation of the $S^{\mathrm{eff}}_{k_1 k_2 p}(\vartheta, \varphi, \theta)$ coefficients. This excursion into the theory turned up the fact that a rigorous justification of an important step in the theoretical description of single crystal perturbation functions with non-axial symmetry had not been presented before, at least at the level of generality necessary for non-axiaiiy symmetric efg's in single crystals. Most previous PAC experiments have used powder sources, considered the efg to be symmetrical, or dealt only with magnetic interactions. The second paper submitted, *Symmetry Property of the Electric Quadrupole Perturbation Function in Gamma Ray Angular Correlations*, presents a rigorous justification of a theoretical procedure for static electric quadrupoie interactions in this most general case.

In the third paper, *The Electric Quadrupole Interaction at Sites of ^{19}F Implants in the four characteristic types of natural Diamond*, an enhancement of the sensitivity of the TDPAD method to slight polycrystalline effects in single crystals for certain geometries is used to investigate the type (impurity and defect) dependence of the efg. Essentially the same two residence sites were found for the other three diamond types as for diamond IIb. This was not suprising as no trapping effects are expected to occur in the ^{19}F recoil implantation time window. However, macroscopic effects were observed,

and these correlated well with the different concentrations of impurities and defects in the different diamond types.

The fourth paper, *The electric quadrupole moment at ^{19}F in Diamond*, submitted reports on cluster calculations on two possible site locations for ^{19}F in diamond. These calculations were extremely significant for the interpretation of subsequent ^{19}F data. From here on, a consistent picture begins to emerge.

The results on the variation of the efg parameters with temperature are presented in the fifth paper submitted: *Temperature dependence study of ^{19}F implants in Diamond by TDPAD*. The temperature dependent behaviour of the ^{19}F defects in diamond both confirm and illuminate the site assignments of the cluster model molecular orbital calculations. Chemical processes are shown to be extremely important for host-impurity interactions in semiconductors and insulators. Our data also support trends in the current interpretation of the dynamics of the host-impurity efg. There is a strong possibility that a large percentage of the ^{19}F is in substitutional sites in diamond with a hole gap state close to the valence band.

Measurements on the other allotropes of carbon are reported on in the last paper: *Residence Sites of ^{19}F Implants in Carbon Allotropes*. The similarity of the local efg at the ^{19}F residence sites in the other carbon allotropes to the ^{19}F sites in diamond show the dominance of chemical effects in determining local efg's.

PAPER 1

Residence Sites for ^{19}F Ions Implanted into Diamond

S CONNELL, K BHARUTH-RAM, H APPEL, JPF SELLSCHOP AND M STEMMET.

Author Connell S H
Name of thesis Internal Fields in Diamond and Related Materials 1988

PUBLISHER:
University of the Witwatersrand, Johannesburg
©2013

LEGAL NOTICES:

Copyright Notice: All materials on the University of the Witwatersrand, Johannesburg Library website are protected by South African copyright law and may not be distributed, transmitted, displayed, or otherwise published in any format, without the prior written permission of the copyright owner.

Disclaimer and Terms of Use: Provided that you maintain all copyright and other notices contained therein, you may download material (one machine readable copy and one print copy per page) for your personal and/or educational non-commercial use only.

The University of the Witwatersrand, Johannesburg, is not responsible for any errors or omissions and excludes any and all liability for any errors in or omissions from the information on the Library website.